PCCP

Physical Chemistry Chemical Physics

rsc.li/pccp

25 YEARS ANNIVERSARY

Alcohol Ammoxidation

ROYAL SOCIETY OF CHEMISTRY

PAPER
Satoshi Muratsugu, Mizuki Tada *et al.*
Low-temperature redox activity and alcohol ammoxidation performance on Cu- and Ru-incorporated ceria catalysts

PCCP Owner Societies

Check for updates

Low-temperature redox activity and alcohol ammoxidation performance on Cu- and Ru-incorporated ceria catalysts†

Chaoqi Chen,[a] Satoru Ikemoto,[a] Gen-ichi Yokota,[a] Kimitaka Higuchi,[b] Satoshi Muratsugu [ID] *[ac] and Mizuki Tada [ID] *[acd]

Transition-metal-incorporated cerium oxides with Cu and a small amount of Ru ($Cu_{0.18}Ru_{0.05}CeO_z$) were prepared, and their low-temperature redox performance (< 423 K) and catalytic alcohol ammoxidation performance were investigated. Temperature-programmed reduction/oxidation under H_2/O_2 and *in situ* X-ray absorption fine structure revealed the reversible redox behavior of the three metals, Cu, Ru, and Ce, in the low-temperature redox processes. The initially reduced Ru species decreased the reduction temperature of Cu oxides and promoted the activation of Ce species. $Cu_{0.18}Ru_{0.05}CeO_z$ selectively catalyzed the production of benzonitrile in the ammoxidation of benzyl alcohol. H_2-treated $Cu_{0.18}Ru_{0.05}CeO_z$ showed a slightly larger initial conversion of benzyl alcohol than O_2-treated $Cu_{0.18}Ru_{0.05}CeO_z$, suggesting that the reduced structure of $Cu_{0.18}Ru_{0.05}CeO_z$ was active for the ammoxidation. The integration of both Cu and Ru resulted in the efficient promotion of ammoxidation, in which the Ru species were involved in the conversion of benzyl alcohol and Cu species were required for selective production of benzonitrile.

Introduction

Transition metal-incorporated cerium oxides (cerias) are promising candidates for catalysts that contain cooperating multiple metal species.[1–3] The metal ion species create oxygen species that are more labile and oxygen vacancy sites on the surface that enhance the redox performance of ceria and are the active sites that generate the unique catalytic performance.[4–10] For instance, it was reported that the deposition of Au species to form $Au/Ce_xZr_{1−x}O_2$ improved the physicochemical properties of $Ce_xZr_{1−x}O_z$. The Au species assisted the distribution of metal particles and also affected the Lewis/Brønsted acidity, which enhanced catalyst selectivity in the

oxidation of 5-hydroxymethylfurfural.[11] The catalyst 1%Pt–1%Co/CeO_2 was prepared by combining a noble metal (Pt) and a 3d transition metal (Co), and the addition of Co altered the chemical states of Pt. This alternation resulted in catalytic activity in hydrogen-borrowing amination by facilitating dehydrogenation and resisting overhydrogenation.[12] The singly dispersed Ni and Ru cations on CeO_2 were developed to enhance the reforming of CH_4 with H_2O. This combination promoted the synergistic effect of Ni activated C–H and Ru activated H_2O to form CO and H_2.[13] We reported that Cr- and Rh-incorporated ceria, $Cr_{0.19}Rh_{0.06}CeO_z$, showed superior redox performance at low temperatures (< 373 K) compared with pure ceria.[14–16] $Cr_{0.19}Rh_{0.06}CeO_z$ exhibited the redox performance of all three metal species and had remarkable NO reduction performance toward N_2 because Rh activated the CO and NO species and Cr cleaved NO species.[14,15] Thus, incorporating multiple metal species into ceria surface leads to efficient oxidation catalysis.

Nitriles, one of the most important organic chemical groups, are used in many industrial applications, such as building blocks for high-performance polymers, useful organic intermediates in pharmaceuticals, and fine chemicals in agriculture.[17–21] Traditionally, nitriles have been produced by the Sandmeyer reaction, Wittig reaction, and cyanation of aryl halides with metal cyanides, all of which share major disadvantages, including the use of toxic reagents, harsh reaction

[a] *Department of Chemistry, Graduate School of Science, Nagoya University, Furo-cho, Chikusa-ku, Nagoya, Aichi 464-8602, Japan. E-mail: muratsugu.satoshi.a5@f.mail.nagoya-u.ac.jp*

[b] *Institute of Materials and Systems for Sustainability, Nagoya University, Furo-cho, Chikusa-ku, Nagoya, Aichi 464-8602, Japan*

[c] *Integrated Research Consortium on Chemical Sciences (IRCCS), Nagoya University, Furo-cho, Chikusa-ku, Nagoya, Aichi 464-8602, Japan*

[d] *Research Center for Materials Science (RCMS), Nagoya University, Furo-cho, Chikusa-ku, Nagoya, Aichi 464-8602, Japan. E-mail: tada.mizuki.u6@f.mail.nagoya-u.ac.jp*

This journal is © the Owner Societies 2024

Phys. Chem. Chem. Phys., 2024, **26**, 17979–17990 | 17979

conditions, and formation of harmful waste.[22–25] Ammoxidation is a reaction that shows promise to address recent shortages of nitriles by forming nitriles directly from the corresponding alcohols and hydrocarbons.[17,26] Ammoxidation uses O_2 and NH_3 as the oxidant and nitrogen source, respectively, and produces H_2O as the only by-product.[17,26] Compared with other functional groups, alcohols have attracted attention as reactants because they can be obtained easily as derivatives from biomass with high stability.[18–20] Pioneering research identified Cu-based and Fe-based homogeneous catalysts with catalytic activity in the ammoxidation of alcohol, although they usually suffer from a low substrate-to-catalyst ratio, difficult separation, and the need for additives, such as 2,2,6,6-tetramethylpiperidine-1-oxyl (TEMPO).[27–31] Heterogeneous catalysts, such as noble metal-based oxides (Ru,[32,33] Pt,[34] and Ag[35]) and transition metal-based carbon (Co,[36,37] Fe,[37,38] La,[39] and Mn[40]), also produce benzonitrile. However, the ammoxidation performance of multiple metal species and the role of metal species in each reaction step are still unrevealed.

In this paper, we report new ceria catalysts containing Cu and a trace amount of Ru (denote as $Cu_{0.18}Ru_{0.05}CeO_z$) for efficient ammoxidation catalysis. $Cu_{0.18}Ru_{0.05}CeO_z$ showed superior redox performance at low temperatures near 373 K and efficient catalytic performance for the ammoxidation of benzyl alcohol. Temperature-programmed reduction/oxidation (TPR/TPO) under H_2/O_2 and *in situ* X-ray absorption fine structure (XAFS) showed that the incorporation of the Ru species shifted the activation of Cu to a lower temperature range, which also contributed to the activation of Ce species. The reduced $Cu_{0.18}Ru_{0.05}CeO_z$ exhibited activity for the selective conversion of benzyl alcohol to benzonitrile, and the reversible redox reaction of $Cu_{0.18}Ru_{0.05}CeO_z$ was suggested to be related to the ammoxidation catalysis with ceria containing the two cooperating transition metal species.

Results and discussion

Structure of $Cu_{0.18}Ru_{0.05}CeO_z$

$Cu_{0.18}Ru_{0.05}CeO_z$ and reference compounds ($Cu_{0.18}CeO_z$, $Ru_{0.04}CeO_z$, CeO_z) were prepared by a hydrothermal method using three metal precursors, ($Cu(NO_3)_2 \cdot 3H_2O$, $RuCl_3$, and $Ce(NO_3)_3 \cdot 6H_2O$) simultaneously, similar to our previous work on $Cr_{0.19}Rh_{0.06}CeO_z$.[14,15] The XRD patterns of as-prepared $Cu_{0.18}Ru_{0.05}CeO_z$ and CeO_z prepared without Ru and Cu showed a similar peak position for the (111) CeO_2 fluorite structure at 28.6° ($Cu_{0.18}Ru_{0.05}CeO_z$) and 28.5° (CeO_z), and there were no major peaks attributed to Ru and Cu compounds (Ru, RuO_2, Cu, and CuO) in the XRD pattern of $Cu_{0.18}Ru_{0.05}CeO_z$ (Fig. 1(a)). The negligible shift of the CeO_2 (111) peak of the
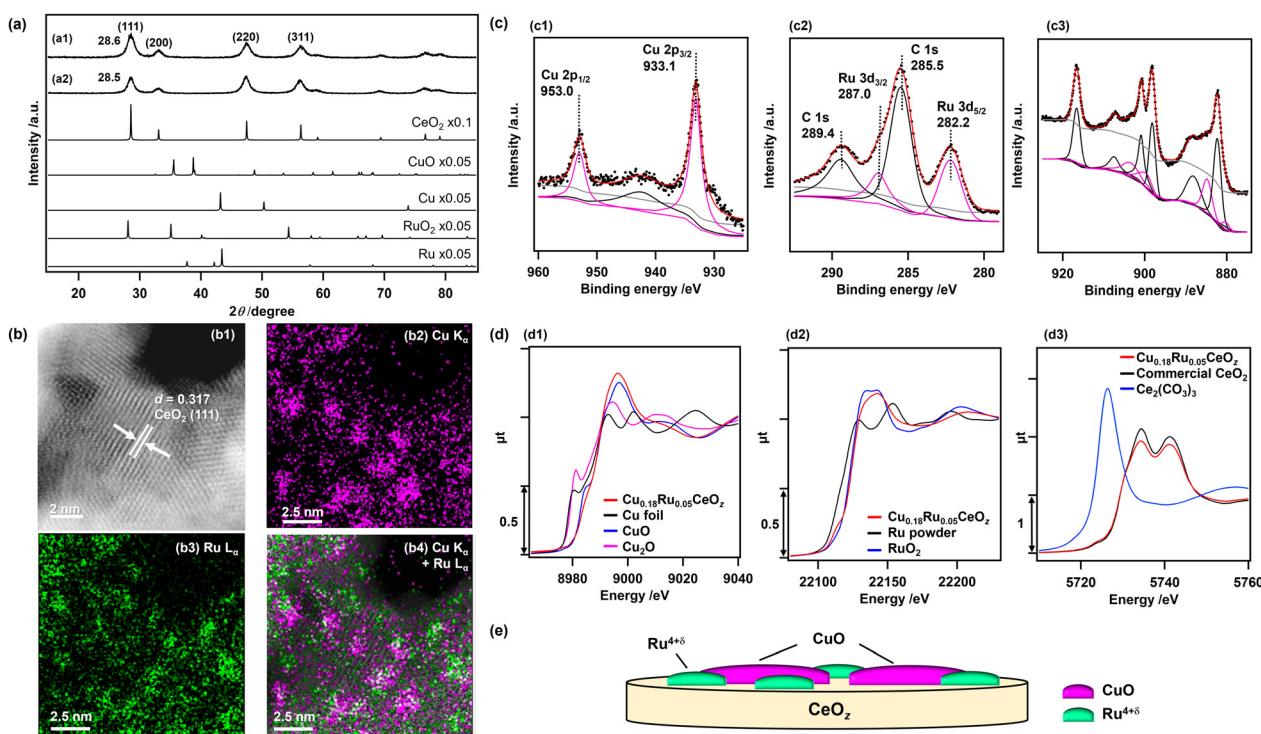
Fig. 1 (a) XRD patterns of (a1) $Cu_{0.18}Ru_{0.05}CeO_z$ and (a2) CeO_z. (b) HAADF-STEM-EDS images of $Cu_{0.18}Ru_{0.05}CeO_z$. (b1) HAADF-STEM image of $Cu_{0.18}Ru_{0.05}CeO_z$, (b2) EDS mapping of Cu, (b3) EDS mapping of Ru, and (b4) overlapped EDS mapping of Cu and Ru. (c) (c1) Cu 2p, (c2) Ru 3d, and (c3) Ce 3d XPS spectra of $Cu_{0.18}Ru_{0.05}CeO_z$. Black dots: observed spectra; red lines: total fitted curves; gray lines: Shirley backgrounds. (c1) Pink line: fitted curves attributed to CuO species; black line: fitted curves attributed to satellite peaks. (c2) Pink line: fitted curves attributed to $Ru^{4+\delta}$ species; black line: fitted curves attributed to C 1s overlapped in the Ru 3d spectrum. (c3) Black line: fitted curves attributed to Ce^{4+} species; pink line: fitted curves attributed to Ce^{3+} species. (d) (d1) Cu K-edge, (d2) Ru K-edge, and (d3) Ce L_{III}-edge XANES spectra of $Cu_{0.18}Ru_{0.05}CeO_z$ with standard reference samples. (e) Schematic of the surface structure of as-prepared $Cu_{0.18}Ru_{0.05}CeO_z$.

17980 | *Phys. Chem. Chem. Phys.*, 2024, **26**, 17979–17990

This journal is © the Owner Societies 2024

prepared $Cu_{0.18}Ru_{0.05}CeO_z$ sample suggested that doping of Cu and Ru into the CeO_2 fluorite structure was negligible.

The Cu, Ru, and Ce contents in $Cu_{0.18}Ru_{0.05}CeO_z$ were determined by inductively coupled plasma-optical emission spectroscopy (ICP-OES) (Table S1, ESI†). The BET surface area of $Cu_{0.18}Ru_{0.05}CeO_z$ was estimated to be 1.24×10^2 m^2 g^{-1}, which was similar to that of CeO_z (1.20×10^2 m^2 g^{-1}) (Table S1, ESI†). Transmission electron microscopy (TEM) (Fig. S1, ESI†) and high-angle annular dark-field scanning transmission electron microscopy (HAADF-STEM) (Fig. 1(b1)) of $Cu_{0.18}Ru_{0.05}CeO_z$ showed a lattice image ($d = 0.317$ nm) that matched the (111) facet of fluorite CeO_2 ($d = 0.312$ nm).[41] HAADF-STEM images with energy dispersive X-ray spectroscopy (EDS) showed the spatial distribution of Cu and Ru on $Cu_{0.18}Ru_{0.05}CeO_z$ and that Cu and Ru were highly dispersed (Fig. 1(b2–b4)). The domain sizes of Cu and Ru species were found to be of nm size as shown in Fig. 1(b).

The oxidation state of Cu in the as-prepared $Cu_{0.18}Ru_{0.05}$-CeO_z sample was characterized by X-ray photoelectron spectroscopy (XPS). The Cu $2p_{3/2}$ XPS peak was observed at 933.1 eV (Fig. 1(c1)) and it agreed with bivalent Cu (933.6 ± 0.4 eV).[42] The slight negative shift of the observed Cu $2p_{3/2}$ peak suggested interaction with the CeO_z surface, such as Cu^{2+}–[O]–Ce (on CeO_2) (reported at 933.0 eV).[43] In addition, a broad satellite peak near 940.0–950.0 eV was observed, which is also characteristic of CuO[44] or Cu^{2+} [45] species (Fig. 1(c1)).

The Ru valence state was estimated by analyzing the energy at the 50% level of the absorption edge of Ru K-edge XANES (Fig. 1(d2)),[46,47] and metallic Ru powder, $Ru(acac)_3$, RuO_2, and $KRuO_4$ with different Ru valence were used as references. The average valence state of Ru in $Cu_{0.18}Ru_{0.05}CeO_z$ was calculated to be +4.5 (Fig. S2 and Table S2, ESI†). The observed Ru $3d_{5/2}$ XPS peak at 282.2 eV (Fig. 1(c2)) agreed with the Ru valence judging from the binding energies of reference compounds (279.9 (Ru^0), 281.4 (RuO_2), and 282.4 eV (RuO_3)).[48]

The oxidation state of Ce was characterized by Ce 3d and O 1s XPS spectra. The Ce 3d XPS spectrum of as-prepared $Cu_{0.18}Ru_{0.05}CeO_z$ (Fig. 1(c3)) were deconvoluted to Ce 3d peaks of Ce^{3+} and Ce^{4+} (see Experimental section and the ESI†). The ratio of the summed peak areas of Ce^{3+} and Ce^{4+} was 0.27/0.73, suggesting that there was a significant amount of reduced Ce^{3+} species at the oxide surface (Table S3, ESI†).[41] The Ce L_{III}-edge XANES spectrum of as-prepared $Cu_{0.18}Ru_{0.05}CeO_z$ showed slight differences in the XANES region from that of commercial CeO_2 (Fig. 1(d3)), and the average oxidation state of Ce was estimated to be +3.85 from the curve-fitting analysis of the Ce L_{III}-edge XANES spectra of commercial CeO_2 and $Ce_2(CO_3)_3$ (Fig. S3, ESI†). The O 1s spectra contained two peaks, which were attributed to the lattice oxygen of CeO_2 (529.6 eV),[14] and either hydroxyl groups or oxygen vacancies that were generated from Ce^{3+} of CeO_2 (531.7 eV)[49,50] (Fig. S4, ESI†).

The curve-fitting analysis of extended X-ray absorption fine structure (EXAFS) Fourier transforms suggested the local coordination structures of Cu and Ru in as-prepared $Cu_{0.18}Ru_{0.05}$-CeO_z. Cu–O bonds at 0.196 ± 0.002 nm (coordination number [CN] of Cu–O: 4.6 ± 1.2) and Ru–O bonds at 0.194 ± 0.002 nm

(CN of Ru–O: 3.2 ± 1.0) were found (Fig. S5, S6 and Tables S4–S7, ESI†). These structural characterization studies indicated that Cu and Ru were not incorporated into the CeO_2 fluorite framework and bivalent Cu oxide and $Ru^{4+\delta}$ oxide were highly dispersed on the surface of CeO_z as nm-sized domain structures illustrated in Fig. 1(e).

Redox properties of $Cu_{0.18}Ru_{0.05}CeO_z$

The redox properties of $Cu_{0.18}Ru_{0.05}CeO_z$ were investigated by using TPR with H_2 and the amounts of H_2 consumed were estimated (Fig. 2 and Table S8, ESI†). The first reduction of as-prepared $Cu_{0.18}Ru_{0.05}CeO_z$ began at 333 K and contained two TPR peaks near 353 and 363 K ("First" in Fig. 2(b)). The H_2 consumption in the first reduction of $Cu_{0.18}Ru_{0.05}CeO_z$ was calculated to be 2.39 mmol g_{cat}^{-1} (Fig. 2(a) and Table S8, ESI†). In contrast, the first TPR of $Cu_{0.18}CeO_z$ showed different features from that of $Cu_{0.18}Ru_{0.05}CeO_z$; the reduction started at around 423 K and the H_2 consumption was smaller than that of $Cu_{0.18}Ru_{0.05}CeO_z$ (1.44 mmol g_{cat}^{-1}) up to 523 K. For $Ru_{0.04}CeO_z$,
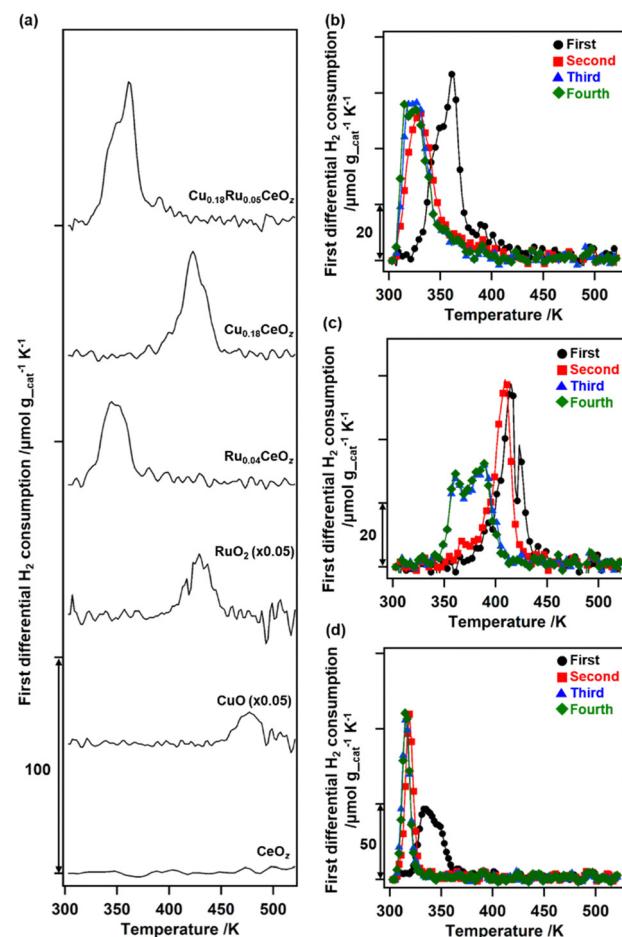
Fig. 2 (a) The first differential plots of the TPR measurements with H_2 of $Cu_{0.18}Ru_{0.05}CeO_z$, $Cu_{0.18}CeO_z$, $Ru_{0.04}CeO_z$, RuO_2, CuO, and CeO_2. First differential plots of continuous TPR with H_2 on (b) $Cu_{0.18}Ru_{0.05}CeO_z$, (c) $Cu_{0.18}CeO_z$, and (d) $Ru_{0.04}CeO_z$ (black: first cycle; red: second cycle; blue: third cycle; green: fourth cycle). TPR was conducted from 303 to 523 K, and TPO was conducted from 303 to 573 K after TPR up to 523 K.

This journal is © the Owner Societies 2024

Phys. Chem. Chem. Phys., 2024, **26**, 17979–17990 | **17981**

the reduction occurred in the low-temperature range, as for $Cu_{0.18}Ru_{0.05}CeO_z$ at 339 K, but H_2 consumption was only 1.60 mmol g_{cat}^{-1}, which was only 67% of that of $Cu_{0.18}Ru_{0.05}$-CeO_z. CeO_z prepared *via* a similar method was not reduced at less than 673 K,[14] and CuO and RuO_2 were reduced at 477 and 429 K, respectively. These results indicated that incorporating Cu and Ru into $Cu_{0.18}Ru_{0.05}CeO_z$ contributed to decreasing the reduction temperature and enhancing its redox properties in the low-temperature range (303–523 K).

After the first TPR, the reduced sample was re-oxidized with O_2 and the amount of O_2 consumption was estimated. The oxidation of $Cu_{0.18}Ru_{0.05}CeO_z$ started at 303 K and 0.92 mmol g_{cat}^{-1} of O_2 was consumed on $Cu_{0.18}Ru_{0.05}CeO_z$ below 573 K (Table S8, ESI†). The O_2 consumption was comparable to the H_2 consumption in the first reduction.

We repeated the reduction and oxidation cycles on $Cu_{0.18}Ru_{0.05}CeO_z$ (Fig. 2(b)). In the second TPR cycle, a large shift in the reduction temperature was observed at 333 K and the trend was reversible for the third and fourth reduction cycles (Fig. 2(b) and Table S8, ESI†). For $Cu_{0.18}CeO_z$ without Ru, the second cycle was similar to the first cycle but third and fourth cycles were different (Fig. 2(c) and Table S8, ESI†). For $Ru_{0.04}CeO_z$, the peak shift was observed in the second cycle and the H_2 consumption was also decreased after the second TPR cycle (Fig. 2(d) and Table S8, ESI†). These results suggested that the incorporation of Cu and Ru into CeO_z not only affected the reversible redox properties of $Cu_{0.18}Ru_{0.05}CeO_z$ but also contributed to the increase in the redox capacity of $Cu_{0.18}Ru_{0.05}CeO_z$.

Changes in the oxidation states of Ru, Cu, and Ce in $Cu_{0.18}Ru_{0.05}CeO_z$ during the TPR/TPO cycles

Changes in the oxidation state of each metal species on as-prepared $Cu_{0.18}Ru_{0.05}CeO_z$ during TPR and TPO were investigated by *in situ* XANES analyses. In the first H_2 reduction, all the *in situ* Ru K-edge, Cu K-edge, and Ce L_{III}-edge XANES spectra of as-prepared $Cu_{0.18}Ru_{0.05}CeO_z$ changed between 303 and 473 K (Fig. 3). The Ru K-edge XANES spectra initially changed at 333 K; the lowest reduction temperature among the metal species. Followed by the reduction of Ru, changes in the Cu K-edge XANES spectra were observed at 353 K and the Ce L_{III}-edge XANES spectra changed at 373 K (Fig. 3(a–c)). The quantitative analyses of the oxidation states of Ru, Cu, and Ce from the XANES spectra revealed that the average oxidation state of Ru changed from +4.37 to +1.06, that of Cu changed from +2.00 to +0.30, and that of Ce changed from +3.85 to +3.62, respectively (Fig. 3(d) and Fig. S7, Tables S9–S11, ESI†). The sum of the oxidation state changes in the three metal species was converted to the H_2 consumption required for reduction (1.81 H_2 mmol g_{cat}^{-1}) (Table S12, ESI†), which was comparable to that observed by TPR measurements (1.9–2.4 H_2 mmol g_{cat}^{-1}). These results strongly suggested that Cu, Ru, and surface Ce species cooperated in the reduction of $Cu_{0.18}Ru_{0.05}CeO_z$, similar to $Cr_{0.19}Rh_{0.06}CeO_z$.[14]

The *in situ* Ru K-edge, Cu K-edge, and Ce L_{III}-edge XANES spectra in the first reoxidation after the TPR measurement were similarly evaluated (Fig. 3(e–g)). Instantaneous oxidation

occurred on Ru and Ce at 303 K, whereas the oxidation of Cu proceeded steadily from 303 K to 573 K. We also plotted the changes in the oxidation states of Cu, Ru, and Ce (Fig. 3(h)), showing the reversible changes on $Cu_{0.18}Ru_{0.05}CeO_z$. The average oxidation states of Ru and Ce changed immediately to +4.40 (Ru) and to +3.83 (Ce) (Fig. 3(h) and Tables S9, S11, ESI†), respectively. The average oxidation state of Cu gradually reverted to +2.00 (Fig. 3(h) and Fig. S7, Table S10, ESI†). Thus, the structural transformation occurred rapidly on Ru and the surface layer of CeO_z, followed by the gradual oxidation of Cu. This behaviour was also similar to $Cr_{0.19}Rh_{0.06}CeO_z$.[14]

We investigated the *in situ* Ru K-edge, Cu K-edge, and Ce L_{III}-edge XANES measurements for the second reduction of $Cu_{0.18}Ru_{0.05}CeO_z$ under H_2 flow conditions (Fig. 3(i–k)). The oxidation states of Ru, Cu, and Ce were again changed to +0.19, +0.29, and +3.62, respectively (Fig. 3(l) and Fig. S7, Tables S9–S11, ESI†). The sum of the H_2 consumption for the second reduction was calculated to be 1.85 H_2 mmol g_{cat}^{-1} (Table S12, ESI†), which was in agreement with the result from the second TPR cycle (1.98 mmol g_{cat}^{-1}). The *in situ* XANES analysis suggested that Ru promoted the subsequent reduction of Cu and Ce species in the reduction.

Changes in the local coordination structures of Ru and Cu in $Cu_{0.18}Ru_{0.05}CeO_z$ during the TPR/TPO cycles

The changes in the local coordination structures of both Cu and Ru species on $Cu_{0.18}Ru_{0.05}CeO_z$ during the TPR/TPO cycles were investigated by the Cu K-edge and Ru K-edge EXAFS curve-fitting analyses (Fig. 4(a), (b) and Fig. S8, S9, Table S13, ESI†). After the H_2 reduction, the Cu K-edge EXAFS changed completely from that of the as-prepared sample; the Cu–O bonds disappeared, and a new peak attributed to Cu–Cu bonds was observed at 0.253 ± 0.001 nm (CN = 6.1 ± 0.9). The Cu–Cu bond peak was similar to that of bulk Cu (0.256 nm) and the EXAFS results suggested the transformation to metallic Cu nanoparticles after the reduction with H_2 (Fig. 4(a2) and Fig. S8, Table S13, ESI†). The Ru K-edge EXAFS after the H_2 reduction showed the appearance of the peak of Ru–Ru bonds (0.2–0.3 nm in the Fourier transform spectra) (Fig. 4(b2), (b6) and Fig. S9, ESI†), suggesting the formation of small metallic Ru nanoclusters.

After the reoxidation, the Cu species reverted to the local coordination structure before the introduction of H_2, with a Cu–O bond at 0.196 ± 0.002 nm (CN = 4.7 ± 0.8) (Fig. 4(a3) and Fig. S8, Table S13, ESI†). The peak of Ru–O bonds (0.1–0.18 nm) became also dominant (Fig. 4(b3) and Fig. S9, ESI†). A similar EXAFS analysis was also conducted after repeating the reduction/oxidation cycles (Fig. 4(a4), (a5), (b4), (b5) and Fig. S8, S9, Table S13, ESI†). After the reduction, Cu–Cu bonds were observed and the Cu–O bonds were consumed after the third oxidation cycle. A similar reversible feature on the structural changes on Ru was observed in the third reduction and oxidation cycles, suggesting drastic structural changes in both Cu and Ru during the reversible redox cycles of $Cu_{0.18}Ru_{0.05}CeO_z$.

Based on the TPR/TPO results and the *in situ* XAFS characterization, the redox structural transformation of $Cu_{0.18}Ru_{0.05}CeO_z$ was proposed as follows (Fig. 5).
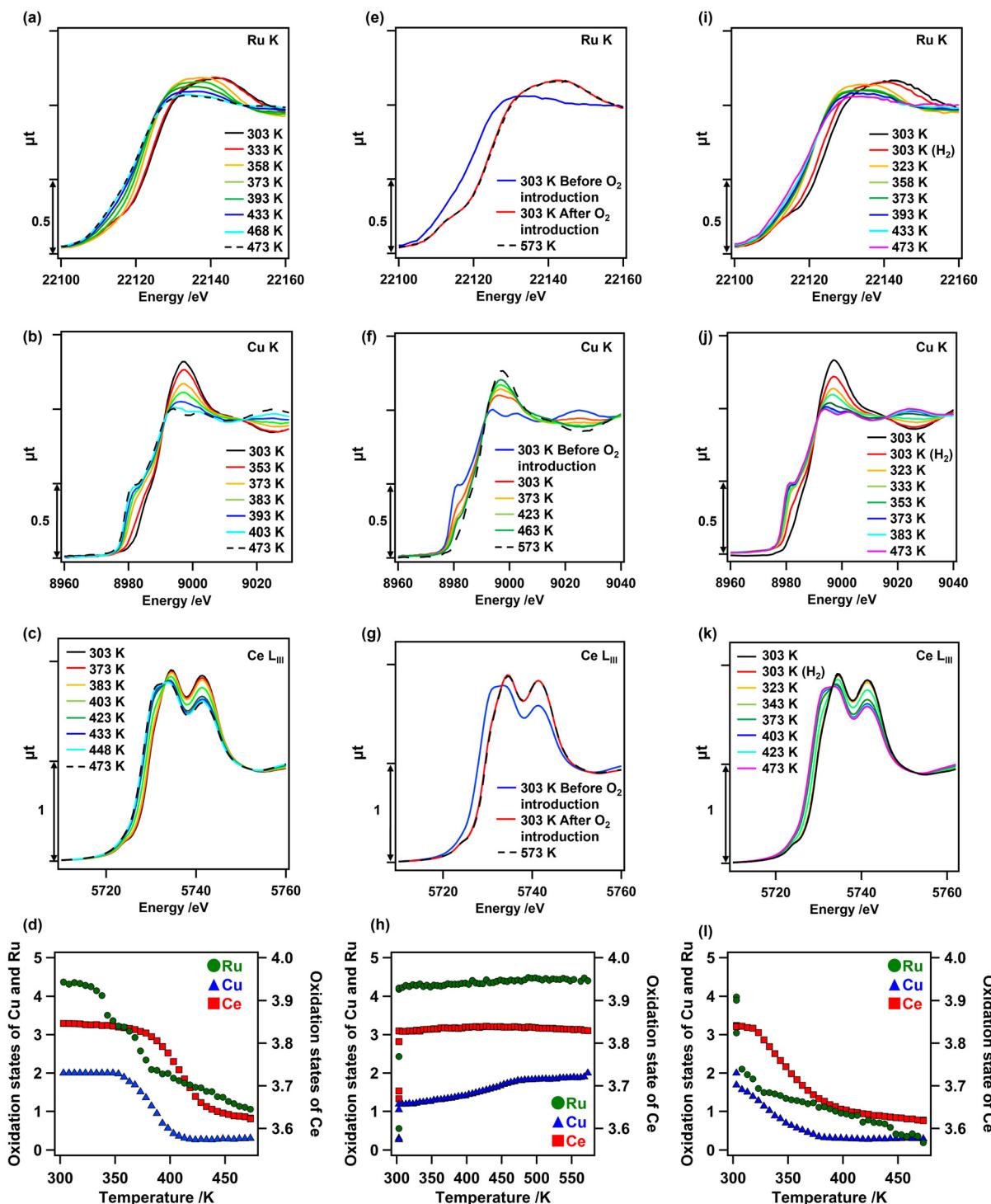
17982 | *Phys. Chem. Chem. Phys.*, 2024, **26**, 17979–17990

This journal is © the Owner Societies 2024

Fig. 3   *In situ* (a) Ru K-edge, (b) Cu K-edge, and (c) Ce L_{III}-edge XANES spectra of $Cu_{0.18}Ru_{0.05}CeO_z$ under H_2 reduction conditions ($H_2 + N_2$, 50 + 50 sccm) from 303 to 473 K (black solid lines: 303 K before reduction; black dashed lines: 473 K under H_2). (d) Changes in the oxidation states of Ru (green), Cu (blue), and Ce (red) calculated from the XANES spectra (a–c) for the first reduction. *In situ* (e) Ru K-edge, (f) Cu K-edge, and (g) Ce L_{III}-edge XANES spectra of $Cu_{0.18}Ru_{0.05}CeO_z$ under O_2 oxidation conditions ($O_2 + N_2$, 50 + 50 sccm) from 303 to 573 K (blue solid lines: 303 K before O_2 introduction; red solid lines: 303 K after O_2 introduction; black dashed lines: 573 K after holding for 1 h). (h) Changes in the oxidation states of Ru (green), Cu (blue), and Ce (red) calculated from the XANES spectra during the first oxidation. *In situ* (i) Ru K-edge, (j) Cu K-edge, and (k) Ce L_{III}-edge XANES spectral changes of $Cu_{0.18}Ru_{0.05}CeO_z$ under H_2 reduction conditions ($H_2 + N_2$ 50 + 50 sccm) from 303 to 473 K (black solid lines: 303 K before reduction; pink solid lines: 473 K under H_2). (l) Changes in the oxidation states of Ru (green), Cu (blue), and Ce (red) calculated from XANES spectra during the second reduction.
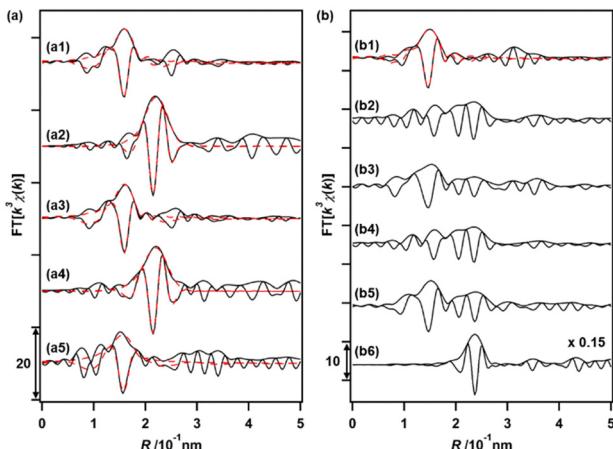
Fig. 4 (a) Cu K-edge EXAFS Fourier transforms of $Cu_{0.18}Ru_{0.05}CeO_z$ ($k =$ 30–140 nm^{-1}); (a1) as-prepared, (a2) after first H_2 reduction, (a3) after first O_2 oxidation, (a4) after third H_2 reduction, and (a5) after third O_2 oxidation. (b) Ru K-edge EXAFS Fourier transforms for $Cu_{0.18}Ru_{0.05}CeO_z$ ($k =$ 30–130 nm^{-1}); (b1) as-prepared, (b2) after first H_2 reduction, (b3) after first O_2 oxidation, (b4) after third H_2 reduction, (b5) after third O_2 oxidation, and (b6) reference Ru powder ($\times 0.15$ in magnitude, $k =$ 30–180 nm^{-1}). H_2 reduction conditions: (27 kPa H_2) from 303 to 523 K, O_2 oxidation conditions: (27 kPa O_2) from 303 to 573 K and held for 2 h after H_2 reduction up to 523 K. Black solid lines showed observed data and red dashed lines with fitted data.

(1) As-prepared $Cu_{0.18}Ru_{0.05}CeO_z$: bivalent Cu oxide and $Ru^{4+\delta}$ oxide were dispersed on the CeO_2 fluorite surface.

(2) After the first reduction in the low-temperature range: Ru oxide was first reduced and converted to metallic Ru nanoclusters at around 333 K. Then, the reduction of Cu and Ce proceeded around 373 K with the formation of Cu nanoparticles and Ce^{3+} species.

(3) After the subsequent oxidation the Ru nanoclusters and surface/subsurface Ce^{3+} species were oxidized quickly at 303 K. Then, the Cu nanoparticles smoothly reverted to Cu oxide at 303–573 K.

(4) Reversible redox transformation after the second cycle: $Cu_{0.18}Ru_{0.05}CeO_z$ was reduced at a lower temperature range than in the first cycle, and the reversible redox transformation between the reduced structure and the oxidized structure was observed.

Ammoxidation performance of benzylic alcohol on $Cu_{0.18}Ru_{0.05}CeO_z$

The catalytic performance of $Cu_{0.18}Ru_{0.05}CeO_z$ for the ammoxidation of benzyl alcohol (**1**) was investigated compared with reference catalysts, such as $Cu_{0.18}CeO_z$, $Ru_{0.04}CeO_z$, and CeO_z
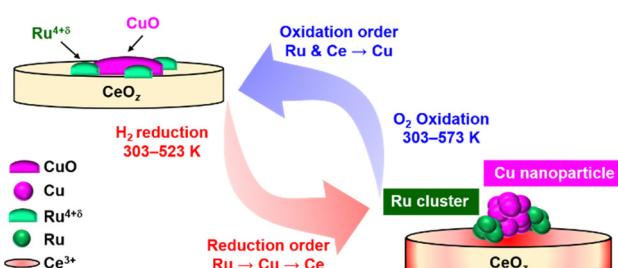
**Fig. 5** Suggested structural transformation of the reversible low-temperature redox cycle of $Cu_{0.18}Ru_{0.05}CeO_z$.

(Table 1). $Cu_{0.18}Ru_{0.05}CeO_z$ showed high benzyl alcohol conversion (95%) with high benzonitrile selectivity (**2a**, 95%) (Table 1, entry 1). Previously reported $Cr_{0.19}Rh_{0.06}CeO_z$[14] showed the conversion of benzyl alcohol (82%), with low benzonitrile selectivity (11%) (Table 1, entry 2). $Cu_{0.18}CeO_z$ without Ru showed lower conversion (70%) and benzonitrile selectivity (78%) than $Cu_{0.18}Ru_{0.05}CeO_z$ (Table 1, entry 3). $Ru_{0.04}CeO_z$ without Cu showed low benzonitrile selectivity (29%), despite the high conversion of benzyl alcohol (91%) (Table 1, entry 4). CeO_z without both Cu and Ru showed low benzonitrile selectivity (10%) (Table 1, entry 5). The physical mixture of $Cu_{0.18}CeO_z$ and $Ru_{0.04}CeO_z$ effectively promoted the reaction (99%) but benzonitrile selectivity was 75% and benzamide was formed (Table 1, entry 6). These results demonstrated that the combination of Cu and Ru on the same CeO_z surface is key for the ammoxidation of benzyl alcohol to benzonitrile, and $Cu_{0.18}Ru_{0.05}CeO_z$ acted as an efficient catalyst for the ammoxidation.

Fig. 6(a) shows the time profiles of benzyl alcohol conversion and selectivity for the products (**2a–2e**) on $Cu_{0.18}Ru_{0.05}CeO_z$. At the beginning of the reaction, a small amount of benzaldehyde was observed, indicating that it was an intermediate in the ammoxidation. Benzonitrile production rate was 2.37×10^{-4} mol g_{cat}^{-1} min^{-1} on $Cu_{0.18}Ru_{0.05}CeO_z$, which was higher than those on $Cu_{0.18}CeO_z$, $Ru_{0.04}CeO_z$, and the physical mixture of $Cu_{0.18}CeO_z$ and $Ru_{0.04}CeO_z$ (Fig. S10(a), ESI)†. The initial reaction rate of benzyl alcohol conversion on $Cu_{0.18}Ru_{0.05}CeO_z$ was also higher than those on $Cu_{0.18}CeO_z$ and $Ru_{0.04}CeO_z$ (Fig. S10(b), ESI†).

The heterogeneity test of $Cu_{0.18}Ru_{0.05}CeO_z$ suggested that the ammoxidation proceeded on the solid catalyst (Fig. S11, ESI†). The recycled $Cu_{0.18}Ru_{0.05}CeO_z$ catalyst (collected by centrifugation and reactivated through calcination at 573 K under air) showed steady performance in the fifth ammoxidation cycle (Fig. 6(b)). ICP-OES showed that negligible amounts of Ru and Ce leaching were observed after each recycling round. The amount of leached Cu after fourth recycling round was approximately 1% of the total amount of Cu in $Cu_{0.18}Ru_{0.05}CeO_z$. $Cu_{0.18}Ru_{0.05}CeO_z$ after the reaction showed a similar XRD pattern to that before (Fig. S12, ESI†). HAADF-STEM-EDS images (Fig. S13, ESI†) and Cu K-edge, Ru K-edge, and Ce L_{III}-edge XANES spectra (Fig. S14, ESI†) were similar to those of the as-prepared catalyst. Cu K-edge and Ru K-edge EXAFS analyses (Fig. S15 and Tables S14, S15, ESI†) also showed a similar local coordination structure to the as-prepared one. These results indicated that $Cu_{0.18}Ru_{0.05}CeO_z$ was stable under the ammoxidation conditions.

We also investigated differences in the ammoxidation activity on reduced and oxidized $Cu_{0.18}Ru_{0.05}CeO_z$. The initial reaction rates of $Cu_{0.18}Ru_{0.05}CeO_z$ after TPR and TPO were measured. $Cu_{0.18}Ru_{0.05}CeO_z$ after treatment with H_2 (after the first TPR) showed higher benzyl alcohol conversion, and $Cu_{0.18}Ru_{0.05}CeO_z$ after treatment with O_2 (after the first TPO) showed similar activity to as-prepared $Cu_{0.18}Ru_{0.05}CeO_z$ (Fig. 6(c)). The differences in the activity between them were clear, and similar differences were also observed for the second TPR and TPO (Fig. 6(c)). The reversibility strongly indicated that the reduced state was more active than the oxidized state for $Cu_{0.18}Ru_{0.05}CeO_z$ and that Ru nanoclusters and

17984 | *Phys. Chem. Chem. Phys.*, 2024, **26**, 17979–17990

This journal is © the Owner Societies 2024

Table 1 Catalytic performance of $Cu_{0.18}Ru_{0.05}CeO_z$ for the ammoxidation of benzyl alcohol and comparison with controls

			2a	2b	2c	2d	2e

Entry	Catalyst	Reaction atmosphere	Conversion of 1%	Select. of 2a %	Select. of 2b %	Select. of 2c %	Select. of 2d %	Select. of 2e %
1^a	$Cu_{0.18}Ru_{0.05}CeO_z$	0.32 MPa NH_3, 1.0 MPa O_2	95	95	5	0	0	3
2^b	$Cr_{0.19}Rh_{0.06}CeO_z$	0.32 MPa NH_3, 1.0 MPa O_2	82	11	21	1	6	3
3^c	$Cu_{0.18}CeO_z$	0.32 MPa NH_3, 1.0 MPa O_2	70	78	11	0	0	4
4^d	$Ru_{0.04}CeO_z$	0.32 MPa NH_3, 1.0 MPa O_2	91	29	12	1	4	12
5^e	CeO_z	0.32 MPa NH_3, 1.0 MPa O_2	76	10	13	1	6	11
6^f	$Cu_{0.18}CeO_z$ + $Ru_{0.04}CeO_z$	0.32 MPa NH_3, 1.0 MPa O_2	99	75	17	0	0	7
7^a	$Cu_{0.18}Ru_{0.05}CeO_z$ (after first TPR)	0.32 MPa NH_3, 1.0 MPa O_2	>99	93	4	0	0	1
8^a	$Cu_{0.18}Ru_{0.05}CeO_z$ (after first TPO)	0.32 MPa NH_3, 1.0 MPa O_2	90	95	6	0	0	2
9	None	0.32 MPa NH_3, 1.0 MPa O_2	0	0	0	0	0	0
10^a	$Cu_{0.18}Ru_{0.05}CeO_z$	1.0 MPa N_2	10	0	0	59	0	46
11^a	$Cu_{0.18}Ru_{0.05}CeO_z$	0.32 MPa NH_3, 1.0 MPa N_2	20	0	0	0	>99	0
12^c	$Cu_{0.18}CeO_z$	0.32 MPa NH_3, 1.0 MPa N_2	9	0	0	0	>99	0
13^d	$Ru_{0.04}CeO_z$	0.32 MPa NH_3, 1.0 MPa N_2	20	4	0	0	66	0
14^e	CeO_z	0.32 MPa NH_3, 1.0 MPa N_2	<1	0	0	0	0	0
15	None	0.32 MPa NH_3, 1.0 MPa N_2	0	0	0	0	0	0

Reaction conditions: **1** (1.93 mmol), toluene (1.0 mL), dodecane (internal standard; 0.07 mL), 423 K, 24 h. The selectivity of **2a–2e** was calculated by product amount/consumed benzyl alcohol amount. Mass balance was over 0.9 except for entries 2, 4, and 5. ^{a} $Cu_{0.18}Ru_{0.05}CeO_z$ (74 mg), Ru/Cu/**1**/NH_3/dodecane = 1/3.5/100/191/100. ^{b} $Cr_{0.19}Rh_{0.06}CeO_z$ (61 mg), Rh/Cr/**1**/NH_3/dodecane = 1/3.5/100/191/100. ^{c} $Cu_{0.18}CeO_z$ (77 mg), Cu/**1**/NH_3/dodecane = 1/29/58/29. ^{d} $Ru_{0.04}CeO_z$ (72 mg), Ru/**1**/NH_3/dodecane = 1/100/191/100. ^{e} CeO_z (74 mg), **1**/NH_3/dodecane = 1/1.91/1. ^{f} $Cu_{0.18}CeO_z$ (77 mg), $Ru_{0.04}CeO_z$ (72 mg), Ru/Cu/**1**/NH_3/dodecane = 1/3.5/100/191/100.

Cu nanoparticles on reduced $Cu_{0.18}Ru_{0.05}CeO_z$ may promote the activation of benzyl alcohol. However, both reduced and oxidized (as-prepared) catalysts showed similar performance for the ammoxidation after 24 h (Table 1, entries 7 and 8); therefore, the ammoxidation proceeded on $Cu_{0.18}Ru_{0.05}CeO_z$ independent of the pretreatment conditions.

Role of Cu and Ru in $Cu_{0.18}Ru_{0.05}CeO_z$ in the ammoxidation of benzyl alcohol

We investigated the activity of lattice oxygen for benzyl alcohol conversion in the absence of O_2. The conversion of benzyl alcohol on $Cu_{0.18}Ru_{0.05}CeO_z$ in the absence of O_2 and NH_3 was only 10% (Table 1, entry 10), and this value, which was equivalent to 1.04 mmol g_{cat}^{-1} of O_2, was comparable to the amount of active lattice oxygen (0.92 mmol g_{cat}^{-1} O_2, from TPR/TPO) (Table S8, ESI†). The reaction of benzyl alcohol with NH_3 in the absence of O_2 also occurred (20% conversion), although the selectivity switched to N-benzylidenebenzamine (**2d**, >99%) (Table 1, entry 11). In contrast, CeO_z showed no conversion of benzyl alcohol (Table 1, entry 14). The Ru K-edge, Cu K-edge, and Ce L_{III}-edge XANES spectra of $Cu_{0.18}Ru_{0.05}CeO_z$ after the reaction suggested that all the metal species changed
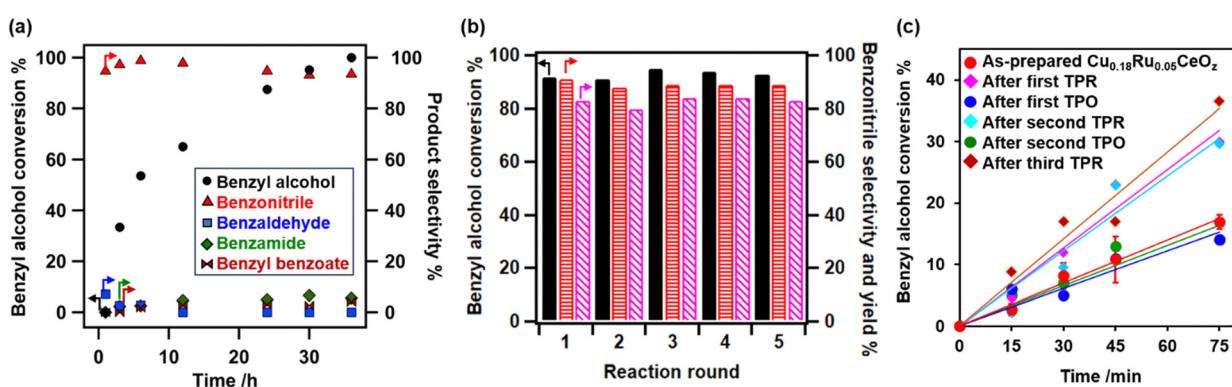
Fig. 6 (a) Time-conversion plots of the ammoxidation of benzyl alcohol on $Cu_{0.18}Ru_{0.05}CeO_z$ at 423 K. (b) Recycling tests for the ammoxidation of benzyl alcohol on $Cu_{0.18}Ru_{0.05}CeO_z$ at 423 K, 24 h (black bars: benzyl alcohol conversion; red horizontal line pattern bars: benzonitrile selectivity; pink diagonal line pattern bars: benzonitrile yield). (c) Initial reaction rates of $Cu_{0.18}Ru_{0.05}CeO_z$ with different pretreatments.

oxidation states (Fig. S16, ESI†). These results demonstrated that the lattice oxygen on $Cu_{0.18}Ru_{0.05}CeO_z$, which was responsible under the redox conditions, involved in the conversion of the alcohol.

The steps in the ammoxidation of benzyl alcohol are the aerobic oxidation of alcohol to form benzaldehyde, self-condensation of the imine through the aldehyde-ammonia interaction, and aerobic oxidation of the imine to form the nitrile.[19] We tested the oxidation of benzyl alcohol, which was the initial step, without the addition of NH_3 (Table S16, ESI†). $Cu_{0.18}Ru_{0.05}CeO_z$ (>99%) and $Ru_{0.04}CeO_z$ (>99%) showed high conversions of benzyl alcohol in the absence of NH_3 with the formation of benzoic acid (Table S16, entries 1 and 3, ESI†). In contrast, $Cu_{0.18}CeO_z$ (30%) and CeO_z (26%) showed moderate conversions of benzyl alcohol with benzaldehyde as the major product, demonstrating that Cu was not mainly responsible for the first benzyl alcohol oxidation (Table S16, entries 2 and 4, ESI†). Thus, Ru was the key element for the first benzyl alcohol oxidation to benzaldehyde.

The second ammoxidation of benzaldehyde was evaluated by the reaction of benzaldehyde with NH_3. The consumption of benzaldehyde occurred without catalysts *via* a spontaneous reaction between benzaldehyde and ammonia,[51] but the selectivity for benzonitrile varied widely among the catalysts (Table S17, ESI†). The benzonitrile selectivity was high for $Cu_{0.18}Ru_{0.05}CeO_z$ (91%) and $Cu_{0.18}CeO_z$ (81%) (Table S17, entries 1 and 2, ESI†), whereas those for $Ru_{0.04}CeO_z$ (5%) and CeO_z (2%) were low (Table S17, entries 3 and 4, ESI†). These results demonstrated that Cu was the active site for benzonitrile formation (Scheme S1, ESI†). Ru species selectively oxidized benzyl alcohol using the lattice oxygen of the catalyst, and then Cu converted the intermediate benzaldehyde to benzonitrile, showing that the incorporation of both Cu and Ru on the same CeO_z surface of $Cu_{0.18}Ru_{0.05}CeO_z$ was required for the selective ammoxidation catalysis.

Conclusions

A Cu- and Ru-incorporated ceria-based catalyst ($Cu_{0.18}Ru_{0.05}CeO_z$) was prepared, and it exhibited low-temperature, reversible redox performance (< 423 K) and high catalytic activity for the ammoxidation of benzyl alcohol to form benzonitrile selectively. *In situ* analysis suggested that the redox behaviors of the mixed oxides were as follows: (i) the reduction of Ru occurred first and promoted the reduction of Cu and Ce below 423 K; and (ii) the oxidation proceeded immediately on Ru and Ce, followed by Cu. The catalytic activity of the benzyl alcohol oxidation depended on the structure of the $Cu_{0.18}Ru_{0.05}CeO_z$ catalyst and the reduced structure was more active than the oxidized structure. The small Ru nanoclusters in the reduced form converted the benzyl alcohol to benzaldehyde, and then the Cu species promoted the formation of benzonitrile with high selectivity. The incorporation of highly dispersed Cu and Ru on the same CeO_z surface of $Cu_{0.18}Ru_{0.05}CeO_z$ (they might be located in close proximity to each other) enhanced the redox properties and the catalytic ammoxidation of benzyl alcohol to benzonitrile.

Experimental

Catalyst preparation

All chemicals were purchased from commercial companies and used without further purification. $Cu(NO_3)_2 \cdot 3H_2O$ (0.67 mmol; Wako), $RuCl_3$ (0.22 mmol; Sigma-Aldrich), and $Ce(NO_3)_3 \cdot 6H_2O$ (3.58 mmol; Sigma-Aldrich) were dissolved in ultrapure water (Milli-Q; 18 mL) and continuously stirred at 293 K for 1 h. Aqueous NaOH solution (7 M, 53 mL) was added to the mixture with continuous stirring for 30 min. The slurry was transferred to a 100 mL Teflon-lined stainless steel vessel autoclave that was sealed and placed in an electric oven and kept at 358 K for 24 h. After the autoclave cooled to room temperature, the precipitate was separated by centrifugation and washed with ultrapure water and ethanol several times followed by drying under air at 353 K for 12 h. The as-dried solid was ground and calcined at 573 K for 2 h to obtain $Cu_{0.18}Ru_{0.05}CeO_z$.

$Cu_{0.18}CeO_z$ and $Ru_{0.04}CeO_z$ were prepared using similar procedures without the addition of the Ru or Cu precursor. CeO_z without Ru and Cu was also prepared using a similar procedure without the Cu and Ru precursors. The hydrothermal temperature of the CeO_z preparation was 373 K, as in our previous paper.[14]

Characterization

XRD. An X-ray diffractometer (MultiFlex, Rigaku; Cu K$_\alpha$, λ = 1.5418 Å, 40 kV, 30 mA, scan rate $2°$ min^{-1}) was used to measure the XRD patterns of the samples at room temperature under air.

ICP-OES. The atomic ratios and compositions of the samples were determined by using ICP-OES (Vista Pro-AX, Varian). Each sample was treated with aqua regia at 353 K for 144 h to fully dissolve the solid powders. A syringe filter (pore size: 0.2 $\mu m\phi$) was used to filter the solution and the solution was diluted with ultrapure water for the ICP-OES measurements. Calibration curves were obtained by diluting the corresponding standard solution with ultrapure water before measuring the prepared samples and were used to estimate the atomic ratios of Cu, Ru, and Ce.

BET. The BET surface area was measured by nitrogen adsorption (Micromeritics ASAP-2020, Shimadzu). Each sample (100 mg) was loaded into a BET cell and degassed under vacuum at 473 K for 2 h before the adsorption measurement. Helium (99.9999%) was used to measure the dead volume after degassing and N_2 adsorption (N_2: 99.99995%) was conducted at 77 K.

TEM and HAADF-STEM-EDS. TEM and HAADF-STEM-EDS images were obtained by using a transmission electron microscope (JEM-ARM 200F, JEOL; High Voltage Electron Microscope Laboratory, Institute of Materials and Systems for Sustainability, Nagoya University, Japan). The accelerating voltage was 200 kV. A powder sample was deposited on a Mo

17986 | *Phys. Chem. Chem. Phys.*, 2024, **26**, 17979–17990

This journal is © the Owner Societies 2024

microgrid. The Mo microgrid with the sample was cleaned with an air duster to remove excess particles before measurements.

XAFS. XAFS spectra at the Cu K-edge and Ce L_{III}-edge were recorded at the BL9C and BL12C stations of the Photon Factory at KEK-IMSS (Tsukuba, Japan) and at the BL5S1 and BL11S2 stations of the Aichi Synchrotron Radiation Center (Seto, Japan). The energy and current of the electrons in the storage ring were 2.5 GeV and 450 mA at the Photon Factory, and 1.2 GeV and 300 mA at the Aichi Synchrotron Center, respectively. X-rays from the storage ring were monochromatized with a Si(111) double-crystal monochromator. At the BL9C and BL12C stations of the Photon Factory, two ionization chambers filled with a mixture of N_2 and He gases (3/7, v/v) and a mixture of N_2 and Ar gases (8.5/1.5, v/v) were used for the Ce L_{III}-edge to monitor the incident (I_0) and transmitted (I) X-rays, respectively. Two ionization chambers filled with pure N_2 and a mixture of pure N_2 and Ar gases (7.5/2.5, v/v) were used for the Cu K-edge to monitor the incident (I_0) and transmitted (I) X-rays, respectively. At the BL5S1 station of the Aichi Synchrotron, two ionization chambers filled with a mixture of N_2/He gases (3/7, v/v) and a mixture of N_2/Ar gases (9.5/0.5, v/v) were used for the Ce L_{III}-edge to monitor the incident (I_0) and transmitted (I) X-rays, respectively. Two ionization chambers filled with pure N_2 and a mixture of pure N_2/Ar gases (7.5/2.5, v/v) were used for the Cu K-edge to monitor the incident (I_0) and transmitted (I) X-rays, respectively. At the BL11S2 station of the Aichi synchrotron, two ionization chambers filled with a mixture of N_2/He gases (4/6, v/v) and a pure N_2 were used for the Ce L_{III}-edge to monitor the incident (I_0) and transmitted (I) X-rays, respectively. Two ionization chambers filled with pure N_2 and a mixture of pure N_2/Ar gases (9/1, v/v) were used for the Cu K-edge to monitor the incident and transmitted X-rays, respectively. Commercial CeO_2 (Sigma-Aldrich; diluted with boron nitride), $Ce_2(CO_3)_3 \cdot xH_2O$ (Sigma-Aldrich; diluted with boron nitride), CuO (Sigma-Aldrich; diluted with boron nitride), Cu_2O (Sigma-Aldrich; diluted with boron nitride), and Cu foil were used as references. As-prepared $Cu_{0.18}Ru_{0.05}CeO_z$ and $Cu_{0.18}Ru_{0.05}CeO_z$ after the ammoxidation (Ce L_{III}-edge: 15 mg, diluted with boron nitride; Cu K-edge: 20 mg, diluted with boron nitride) was ground and packed into a cell (4 mmϕ), and the cell was sealed with a Kapton film under air. $Cu_{0.18}Ru_{0.05}CeO_z$ after the first and third TPR/TPO, and after the ammoxidation under N_2 was ground and packed into a cell (4 mmϕ) in the glove box filled with Ar, and the cell was sealed with a Kapton film under an Ar atmosphere. All samples were measured in transmission mode at 298 K.

XAFS spectra at the Ru K-edge were measured at the NW10A station of the Photon-Factory Advanced Ring (PF-AR) at KEK-IMSS and at the BL11S2 station of the Aichi Synchrotron Radiation Center. The energy and current of the electrons in the storage ring were 6.5 GeV and 60 mA at PF-AR, and 1.2 GeV and 300 mA at the Aichi Synchrotron Center, respectively. X-rays from the storage ring were monochromatized with a Si(311) double-crystal monochromator. At the NW10A station of the Photon Factory, two ionization chambers filled with pure Ar were used to monitor the incident (I_0) and transmitted

(I) X-rays. At the BL11S2 station of the Aichi Synchrotron Center, two ionization chambers filled with pure Ar and a mixture of pure Ar and Kr (9/1, v/v) were used to monitor both the incident (I_0) and transmitted (I) X-rays, respectively. Ru(acac)$_3$ (diluted with boron nitride), RuO_2 (Sigma-Aldrich; diluted with boron nitride), $KRuO_4$ (Sigma-Aldrich; diluted with boron nitride), and Ru powder (diluted with boron nitride) were used as references. As-prepared $Cu_{0.18}Ru_{0.05}CeO_z$ and $Cu_{0.18}Ru_{0.05}CeO_z$ after the ammoxidation (25 mg) were ground and packed into a cell (4 mmϕ), and the cell was sealed with a Kapton film under air. $Cu_{0.18}Ru_{0.05}CeO_z$ after the first and third TPR/TPO, and after the ammoxidation under N_2 was ground and packed into a cell (4 mmϕ) in the glove box filled with Ar, and the cell was sealed with a Kapton film under an Ar atmosphere. All samples were measured in transmission mode at 298 K.

XAFS spectra were analysed using ATHENA and ARTEMIS with IFEFFIT (version 1.2.11).[52,53] Threshold energies were tentatively set at 8980.3 eV (Cu K-edge; the inflection point of Cu foil[54]), 22119.3 eV (Ru K-edge; the inflection point of Ru^0 powder[54]), and 5734.4 eV (Ce L_{III}-edge; the first peak top of the white line for CeO_2), and background was subtracted using the Autobk program and the spline smoothing algorithm in ATHENA.[55,56] The average oxidation states of Ce were determined from the changes at the second peak top of the CeO_2 white line (5741.3 eV). The average oxidation states of Cu were determined by linear combination fitting using the XANES spectra of Cu foil, Cu_2O, and CuO (8960.0–9010.0 eV). The average oxidation states of Ru were determined from the Ru K-edge energy (at the 50% level of the edge jump in the spectrum) *versus* the calibration graph, which was constructed by using Ru powder (+0), Ru(acac)$_3$ (+3), RuO_2 (+4), and $KRuO_4$ (+7) as references for different oxidation states.[46,47]

The k^3-weighted EXAFS oscillation was Fourier transformed into R-space and curve-fitting analysis was performed. For the Cu K-edge, S_0^2 was fixed as 1 for metallic Cu based on the fitting of Cu foil and 0.70 for Cu^{2+} based on the fitting of CuO (Fig. S5 and Table S4, ESI†). For the Ru K-edge, S_0^2 was fixed as 0.86 based on the fitting of RuO_2 (Fig. S5 and Table S5, ESI†). Phase shifts and backscattering amplitudes for Cu–O, Cu–Cu, Ru–O, and Ru–Ru were calculated with FEFF8[57] code by using structural parameters obtained from the crystal structures of CuO (ICSD-16025), Cu (ICSD-53246), RuO_2 (ICSD-23961), and Ru (ICSD-40354). Coordination number (CN), interatomic distance (R), Debye–Waller factor (σ^2, mean-square displacement), and correction-of-edge energy (ΔE) were calculated as fitting parameters for each shell.

XPS. XPS was measured on an X-ray photoelectron spectrometer (Scienta Omicron R4000, base pressure: 4×10^{-8} Pa) with a monochromatized Al K_α X-ray source (Scienta Omicron MX650, photon energy: 1486.7 eV, power: 180 W). $Cu_{0.18}Ru_{0.05}CeO_z$ was ground and pressed into disks (7 mmϕ, 20 mg, pressed at 20 MPa) and attached to the cell holder with carbon tape under air. The cell holder was kept under vacuum overnight until the pressure was lower than 5×10^{-5} Pa and was transferred to the XPS measurement chamber to be measured with a step size of 0.1 eV and a pass energy of 200 eV.

This journal is © the Owner Societies 2024

Phys. Chem. Chem. Phys., 2024, **26**, 17979–17990 | **17987**

The binding energies were referenced to the O 1s peak of CeO_2 lattice oxygen (529.6 eV, Fig. S4, ESI†).[14] The Shirley background was subtracted, and each peak was fitted by using a Voigt function.[58] The deconvolution of Ce 3d XPS spectrum of as-prepared $Cu_{0.18}Ru_{0.05}CeO_z$ (Fig. 1(c3)) revealed the existence of both Ce^{4+} (u''', u'', u_0, v''', v'', and v_0) and Ce^{3+} (u', u_0, v', and v_0).[41,59] The sum of the Ce 3d peak areas of Ce^{3+} and Ce^{4+} were calculated from the deconvoluted Ce 3d XPS spectra.

TPR with H_2 and TPO with O_2. TPR and TPO were performed in a closed glass reactor system, which included a gas circulation unit and a pressure gauge. Typically, a sample (200 mg) was evacuated for 30 min, followed by the introduction of 27 kPa H_2 (99.99999%) into the reactor. Then, the temperature was increased at a rate of 5 K min^{-1}. H_2O formed by sample reduction was trapped with a liquid N_2 trap. The pressure change in the system was recorded at appropriate intervals. After the TPR measurement, TPO was performed by introducing 27 kPa O_2 (99.99995%) into the reactor at 293 K. The system was heated to 573 K (5 K min^{-1}) and kept at 573 K for 2 h. Finally, the pressure change in the system was recorded at appropriate intervals. Desorbed H_2O was trapped with a dry-ice/acetone trap during TPO. After the entire system returned to 293 K, the second and subsequent round of the TPR and TPO measurements were conducted by introducing 27 kPa H_2 or O_2 gas by a similar procedure.

***In situ* XAFS.** *In situ* quick XAFS (QXAFS) measurements were performed under reduction or oxidation conditions at the Photon Factory and PF-AR at KEK-IMSS as follows (The detailed procedures to set up XAFS beamlines are described in the section "XAFS".). A calculated amount of $Cu_{0.18}Ru_{0.05}CeO_z$ for each element (Ru K-edge: 74 mg; Cu K-edge: 63 mg, diluted with boron nitride; Ce L_{III}-edge: 40 mg, diluted with boron nitride) was pelletized into a disk and transferred to an *in situ* XAFS cell (7 mmϕ) (Fig. S17, ESI†). After flushing with N_2 (99.999%, 100 sccm) for 10 min, the cell was heated to 303 K and kept at this temperature for 5 min. Then, the QXAFS measurement was performed. After 5 min, the gas was switched to a mixture of H_2 (99.99999%) and N_2 (50 and 50 sccm) with the temperature maintained for another 5 min. Then, the cell was heated to 473 K at a rate of 2 K min^{-1}. After maintaining the temperature at 473 K for 10 min, the gas was changed back to N_2 (100 sccm), and the cell was cooled to room temperature. Later, the cell was heated again to 303 K and kept at this temperature for 5 min, and the QXAFS measurement was performed. After 5 min, the gas was switched to a mixture of O_2 (99.99995%) and N_2 (50 and 50 sccm), and the temperature was held for another 5 min. Then, the cell was heated to 573 K at a rate of 5 K min^{-1}. After maintaining the temperature at 573 K for 1 h, the gas was changed to N_2 (100 sccm), and the cell was cooled to room temperature. After flushing with N_2 for another 10 min, the second round of the H_2 reduction and O_2 oxidation were performed by following the same procedure above with a simultaneous QXAFS measurement.

Catalytic reactions

Ammoxidation of benzyl alcohol. The ammoxidation of benzyl alcohol was conducted in a high-pressure autoclave equipped with a pressure gauge. Typically, the as-prepared sample ($Cu_{0.18}Ru_{0.05}CeO_z$, 74 mg) was placed in the Teflon tube of autoclave in air, followed by the addition of toluene (1 mL; Wako Super-dehydrated; bubbled with O_2 (99.99995%) for 30 min), and benzyl alcohol (0.2 mL; Wako Special grade; 1.93 mmol, 1.63 mol L^{-1}). The atmosphere of the autoclave was changed to 0.32 MPa of NH_3 (99.999%) and 1.0 MPa of O_2 (99.99995%) and the reaction was performed at 423 K. After the corresponding reaction time, the product was quenched by placing the autoclave in the ice bath. The product was collected by the addition of toluene (0.5 mL; Wako Super-dehydrated) and 1,4-dioxane (4.5 mL; Wako Super-dehydrated). After the catalyst was separated, the product was analysed by FID-GC (GC-2014s, Shimadzu) and GC-MS (GC2010, PARVUM2, Shimadzu) equipped with an InertCap 5 column (GL Science; 0.25 mm (df) × 0.25 mm (ID) × 30 m) and with dodecane (0.07 mL; Wako Special grade) as the internal standard. The molar ratio of Ru/Cu/alcohol/NH_3/dodecane was 1/3.5/100/191/100. Benzyl alcohol conversion, selectivity, and mass balance were calculated by the following equations.

Benzyl alcohol conversion (%) = ((mole of benzyl alcohol)$_{initial}$ − (mole benzyl alcohol)$_{final}$)/(mol of benzyl alcohol)$_{initial}$ × 100%

$$(1)$$

Benzonitrile selectivity (%) = (mole of benzonitrile)$_{final}$/((mole of benzyl alcohol)$_{initial}$ − (mol of benzyl alcohol)$_{final}$) × 100%

$$(2)$$

By-product selectivity (%) = (mole of by-product)$_{final}$/((mole benzyl alcohol)$_{initial}$ − (mol benzyl alcohol)$_{final}$) × 100%

$$(3)$$

Mass balance = ((mole of benzyl alcohol)$_{final}$ + (mole of all products)$_{final}$)/(mol of benzyl alcohol)$_{initial}$

$$(4)$$

To evaluate the ammoxidation performance of different redox phases, $Cu_{0.18}Ru_{0.05}CeO_z$ treated with 27 kPa of H_2 (99.99999%) (denoted as $Cu_{0.18}Ru_{0.05}CeO_z$ after first TPR), and $Cu_{0.18}Ru_{0.05}CeO_z$ treated with 27 kPa of H_2 followed by 27 kPa of O_2 (denoted as $Cu_{0.18}Ru_{0.05}CeO_z$ after first TPO) were prepared (The detailed procedure is described in the section "TPR with H_2 and TPO with O_2".). The sample was transferred into a Teflon tube of the autoclave in an Ar-filled glove box, and toluene and benzyl alcohol (both degassed) were added in the glove box. Then the autoclave was tightly sealed and taken out of the glove box, and the inner atmosphere was changed accordingly.

Benzyl alcohol oxidation was performed using a similar procedure without the addition of 0.32 MPa of NH_3. The ammoxidation of benzaldehyde was performed by changing the starting substrate to benzaldehyde (0.2 mL; Sigma-Aldrich; 1.96 mmol, 1.63 mol L^{-1}). The ammoxidation of benzyl alcohol under a N_2 atmosphere was performed with the addition of all the starting substrates in the Ar-filled glove box. The autoclave was placed under vacuum before the addition of 0.32 MPa of NH_3 and 1.0 MPa of N_2 (99.99995%) to avoid O_2 appearing in the autoclave.

Catalyst recycling test. The scale of the ammoxidation of benzyl alcohol was 1.5 times larger for this experiment. The

17988 | *Phys. Chem. Chem. Phys.*, 2024, **26**, 17979–17990

This journal is © the Owner Societies 2024

recycling of the solid catalyst was performed by washing the catalyst with toluene and centrifuging the solution. After the catalyst was washed several times, it was dried in the oven for 12 h and calcined at 573 K for 2 h under air.

Heterogeneity test and leaching test. After the reaction reached approximately 30% conversion (2 h), the gas in the autoclave was released and the catalyst was removed through hot filtration with a 0.1 μm filter. The solution was transferred to another autoclave to perform the ammoxidation for the rest of the reaction time with the addition of 0.32 MPa of NH_3 and 1.0 MPa of O_2. In addition, the leaching test was performed by collecting the solution after the reaction. The reaction solution was collected in a round bottom flask and evaporated on a rotary evaporator and vacuum line. The remaining precipitate was treated with aqua regia (2 mL) at 353 K for 24 h, and ICP-OES was used to detect the leached metal species.

Author contributions

C. C. prepared catalysts, carried out the redox performance measurements, investigated the ammoxidation reactions, and wrote the manuscript. S. I. contributed to XPS measurements and *in situ* XAFS measurements. G. Y. designed the setup of the redox measurement and evaluation of the ammoxidation reaction. K. H. carried out TEM and HAADF-STEM measurements. S. M. conceived the project and wrote the manuscript. M. T. directed this study.

Conflicts of interest

There are no conflicts to declare.

Acknowledgements

Notes and references

1 T. Montini, M. Melchionna, M. Monai and P. Fornasiero, *Chem. Rev.*, 2016, **116**, 5987–6041.

2 P. Li, X. Chen, Y. Li and J. W. Schwank, *Catal. Today*, 2019, **327**, 90–115.

3 E. W. McFarland and H. Metiu, *Chem. Rev.*, 2013, **113**, 4391–4427.

4 M. Ozawa, M. Kimura and A. Isogai, *J. Alloys Compd.*, 1993, **193**, 73–75.

5 P. Zhang, H. Lu, Y. Zhou, L. Zhang, Z. Wu, S. Yang, H. Shi, Q. Zhu, Y. Chen and S. Dai, *Nat. Commun.*, 2015, **6**, 8446.

6 J. Beckers and G. Rothenberg, *Dalton Trans.*, 2008, 6573–6578.

7 Y. Xiong, L. Li, L. Zhang, Y. Cao, S. Yu, C. Tang and L. Dong, *Phys. Chem. Chem. Phys.*, 2017, **19**, 21840–21847.

8 Y. Guo, S. Mei, K. Yuan, D.-J. Wang, H.-C. Liu, C.-H. Yan and Y.-W. Zhang, *ACS Catal.*, 2018, **8**, 6203–6215.

9 N. C. Nelson, J. S. Manzano, A. D. Sadow, S. H. Overbury and I. I. Slowing, *ACS Catal.*, 2015, **5**, 2051–2061.

10 T. Rajkumar, A. Sápi, M. Ábel, J. Kiss, I. Szenti, K. Baán, J. F. Gómez-Pérez, Á. Kukovecz and Z. Kónya, *Catal. Lett.*, 2021, **151**, 3477–3491.

11 C. Megías-Sayago, K. Chakarova, A. Penkova, A. Lolli, S. Ivanova, S. Albonetti, F. Cavani and J. A. Odriozola, *ACS Catal.*, 2018, **8**, 11154–11164.

12 T. Tong, W. Guo, X. Liu, Y. Guo, C.-W. Pao, J.-L. Chen, Y. Hu and Y. Wang, *J. Catal.*, 2019, **378**, 392–401.

13 Y. Chen, B. deGlee, Y. Tang, Z. Wang, B. Zhao, Y. Wei, L. Zhang, S. Yoo, K. Pei, J. H. Kim, Y. Ding, P. Hu, F. F. Tao and M. Liu, *Nat. Energy*, 2018, **3**, 1042–1050.

14 S. Ikemoto, X. Huang, S. Muratsugu, S. Nagase, T. Koitaya, H. Matsui, G. Yokota, T. Sudoh, A. Hashimoto, Y. Tan, S. Yamamoto, J. Tang, I. Matsuda, J. Yoshinobu, T. Yokoyama, S. Kusaka, R. Matsuda and M. Tada, *Phys. Chem. Chem. Phys.*, 2019, **21**, 20868–20877.

15 S. Ikemoto, S. Muratsugu, T. Koitaya and M. Tada, *ACS Catal.*, 2022, **12**, 431–441.

16 S. Ikemoto, S. Muratsugu, T. Koitaya, Y. Tsuji, M. Das, K. Yoshizawa, F. Glorius and M. Tada, *J. Am. Chem. Soc.*, 2023, **145**, 1497–1504.

17 A. Martin and V. N. Kalevaru, *ChemCatChem*, 2010, **2**, 1504–1522.

18 G. Yan, Y. Zhang and J. Wang, *Adv. Synth. Catal.*, 2017, **359**, 4068–4105.

19 Z. Qi, C. Hu, Y. Zhong, C. Cai and G.-P. Lu, *Org. Chem. Front.*, 2021, **8**, 3137–3149.

This journal is © the Owner Societies 2024

Phys. Chem. Chem. Phys., 2024, **26**, 17979–17990 | **17989**

20 Y. Wang, S. Furukawa, X. Fu and N. Yan, *ACS Catal.*, 2020, **10**, 311–335.

21 J. Kim, H. J. Kim and S. Chang, *Angew. Chem., Int. Ed.*, 2012, **51**, 11948–11959.

22 H. H. Hodgson, *Chem. Rev.*, 1947, **40**, 251–277.

23 V. V. Grushin and H. Alper, *Chem. Rev.*, 1994, **94**, 1047–1062.

24 M. Ezawa and H. Togo, *Eur. J. Org. Chem.*, 2017, 2379–2384.

25 P. Anbarasan, T. Schareina and M. Beller, *Chem. Soc. Rev.*, 2011, **40**, 5049–5067.

26 J. F. Brazdil, *Catal. Today*, 2021, **363**, 55–59.

27 J.-B. Xie, J.-J. Bao, H.-X. Li, D.-W. Tan, H.-Y. Li and J.-P. Lang, *RSC Adv.*, 2014, **4**, 54007–54017.

28 D.-W. Tan, J.-B. Xie, Q. Li, H.-X. Li, J.-C. Li, H.-Y. Li and J.-P. Lang, *Dalton Trans.*, 2014, **43**, 14061–14071.

29 W. Yin, C. Wang and Y. Huang, *Org. Lett.*, 2013, **15**, 1850–1853.

30 G. Zhang, D. Ma, Y. Zhao, G. Zhang, G. Mei, J. Lyu, C. Ding and S. Shan, *ChemistryOpen*, 2018, **7**, 885–889.

31 S. U. Dighe, D. Chowdhury and S. Batra, *Adv. Synth. Catal.*, 2014, **356**, 3892–3896.

32 T. Oishi, K. Yamaguchi and N. Mizuno, *Angew. Chem., Int. Ed.*, 2009, **48**, 6286–6288.

33 H. Wang, D. Xu, E. Guan, L. Wang, J. Zhang, C. Wang, S. Wang, H. Xu, X. Meng, B. Yang, B. C. Gates and F.-S. Xiao, *ACS Catal.*, 2020, **10**, 6299–6308.

34 Y. Preger, T. W. Root and S. S. Stahl, *ACS Omega*, 2018, **3**, 6091–6096.

35 A. N. Hashemi, H. Eshghi and K. Lamei, *Appl. Organomet. Chem.*, 2019, **33**, e4835.

36 F. Mao, Z. Qi, H. Fan, D. Sui, R. Chen and J. Huang, *RSC Adv.*, 2017, **7**, 1498–1503.

37 R. V. Jagadeesh, H. Junge and M. Beller, *Nat. Commun.*, 2014, **5**, 4123.

38 T. Yasukawa, X. Yang and S. Kobayashi, *J. Org. Chem.*, 2020, **85**, 7543–7548.

39 F. Ziaee, M. Gholizadeh and S. M. Seyedi, *Appl. Organomet. Chem.*, 2018, **32**, e4253.

40 T. Ishida, H. Watanabe, T. Takei, A. Hamasaki, M. Tokunaga and M. Haruta, *Appl. Catal., A*, 2012, **425–426**, 85–90.

41 D. R. Mullins, *Surf. Sci. Rep.*, 2015, **70**, 42–85.

42 M. C. Biesinger, *Surf. Interface Anal.*, 2017, **49**, 1325–1334.

43 F. Chen, Y. Xia, J. Lao, D. Cheng and X. Zhan, *Ind. Eng. Chem. Res.*, 2021, **60**, 9068–9079.

44 S. Cao, B. Zou, J. Yang, J. Wang and H. Feng, *ACS Appl. Nano Mater.*, 2022, **5**, 11689–11698.

45 Z. Liu, Q. Wang, J. Wu, H. Zhang, Y. Liu, T. Zhang, H. Tian and S. Zeng, *ACS Appl. Mater. Interfaces*, 2021, **13**, 35804–35817.

46 N. Planas, L. Vigara, C. Cady, P. Miró, P. Huang, L. Hammarström, S. Styring, N. Leidel, H. Dau, M. Haumann, L. Gagliardi, C. J. Cramer and A. Llobet, *Inorg. Chem.*, 2011, **50**, 11134–11142.

47 K. Sardar, E. Petrucco, C. I. Hiley, J. D. B. Sharman, P. P. Wells, A. E. Russell, R. J. Kashtiban, J. Sloan and R. I. Walton, *Angew. Chem., Int. Ed.*, 2014, **53**, 10960–10964.

48 D. J. Morgan, *Surf. Interface Anal.*, 2015, **47**, 1072–1079.

49 Z. Li, K. Werner, K. Qian, R. You, A. Płucienik, A. Jia, L. Wu, L. Zhang, H. Pan, H. Kuhlenbeck, S. Shaikhutdinov, W. Huang and H.-J. Freund, *Angew. Chem., Int. Ed.*, 2019, **58**, 14686–14693.

50 C. Yang, X. Yu, S. Heißler, A. Nefedov, S. Colussi, J. Llorca, A. Trovarelli, Y. Wang and C. Wöll, *Angew. Chem., Int. Ed.*, 2017, **56**, 375–379.

51 J.-M. Huang, J.-F. Zhang, Y. Dong and W. Gong, *J. Org. Chem.*, 2011, **76**, 3511–3514.

52 B. Ravel and M. Newville, *J. Synchrotron Radiat.*, 2005, **12**, 537–541.

53 M. Newville, B. Ravel, D. Haskel, J. J. Rehr, E. A. Stern and Y. Yacoby, *Phys. B*, 1995, **208–209**, 154–156.

54 J. A. Bearden and A. F. Burr, *Rev. Mod. Phys.*, 1967, **39**, 125–142.

55 M. Newville, *J. Synchrotron Radiat.*, 2001, **8**, 322–324.

56 M. Newville, P. Līviņš, Y. Yacoby, J. J. Rehr and E. A. Stern, *Phys. Rev. B: Condens. Matter Mater. Phys.*, 1993, **47**, 14126–14131.

57 A. L. Ankudinov, B. Ravel, J. J. Rehr and S. D. Conradson, *Phys. Rev. B: Condens. Matter Mater. Phys.*, 1998, **58**, 7565–7576.

58 M. Repoux, *Surf. Interface Anal.*, 1992, **18**, 567–570.

59 G. Yan, Y. Tang, Y. Li, Y. Li, L. Nguyen, T. Sakata, K. Higashi, F. F. Tao and P. Sautet, *Nat. Catal.*, 2022, **5**, 119–127.

17990 | *Phys. Chem. Chem. Phys.*, 2024, **26**, 17979–17990

This journal is © the Owner Societies 2024